Materials Horizons

COMMUNICATION

View Article Online
View Journal | View Issue

Cite this: *Mater. Horiz.*, 2018, 5, 961

Received 18th May 2018,
Accepted 23rd July 2018

DOI: 10.1039/c8mh00590g

rsc.li/materials-horizons

A class of Pb-free double perovskite halide semiconductors with intrinsic ferromagnetism, large spin splitting and high Curie temperature†

Bo Cai,[a] Xi Chen,[a] Meiqiu Xie,[a] Shengli Zhang, *[a] Xuhai Liu,[a] Jinlong Yang, [b] Wenhan Zhou,[a] Shiying Guo[a] and Haibo Zeng *[a]

Room-temperature ferromagnetic (FM) semiconductors are of vital importance for realizing advanced spintronic devices. The recent discovery of diluted ferromagnetism in Mn-doped $CH_3NH_3PbI_3$ suggests hopes for developing halide perovskite based spintronics. However, the measured Curie temperature was usually below 15 K, which severely prohibits the Mn-doped $CH_3NH_3PbI_3$ from being applied in room-temperature applications. In this work, instead of using the usual doping strategy, we present a new class of Pb-free FM halide semiconductors with double perovskite structures (Cs_2GeMX_6, transition metal M = V, Mn or Ni; X = Cl, Br or I), which possess spin splitting in a broad range of 0.06–1.00 eV and ultra-high Curie temperature of 490–800 K. Furthermore, the Curie temperature can still be higher than room temperature under the lattice expansion effect. These excellent intrinsic properties are because of the large number of nearest neighboring magnetic ions and strong exchange coupling between the M 3d and GeX_6 σ_{s-p}* orbitals. Our designed Pb-free FM halide semiconductors with double perovskite structures can be envisaged to develop into other highly dynamic research fields with vast implications for high-performance spin optoelectronics and spintronics.

Conceptual insights

As the Moore's law approaches the limit, spintronics has received intensive research interest due to its potential to revolutionize information technology. The utilization of spintronics requires the creation of a ferromagnetic semiconductor that can work at room temperature. Here, we introduce famous photovoltaic/optoelectronic material perovskite halides into the spintronics field. We present a series of intrinsic ferromagnetic semiconductors, namely double perovskite halides with a stable crystalline structure at room temperature. Furthermore, the ferromagnetic compounds are semiconductors with large spin splitting and high Curie temperature, which is crucial for extending the applications of perovskite halides in spintronics.

Introduction

Spintronics has demonstrated great potential in next-generation high speed and low power consumption information technology.[1,2] However, it is still a major challenge to obtain 100% spin polarized carriers at room temperature (RT). Until now, a considerable amount of spintronic materials have been explored, such as europium chalcogenides (EuO, EuS),[3–5] spinel ($NiFe_2O_4$, $CoFe_2O_4$),[6,7] perovskite oxides ($BiFeO_3$) and double perovskite oxides (Bi_2CrOsO_6),[2,8–13] Heusler compounds (CoVTiAl, CoVZrAl)[14] and layered Cr-based materials as well as the corresponding low-dimensional compounds ($CrGeTe_3$ and CrI_3).[15–18] However, their small quantity of spin polarized carriers and low Curie temperature are two critical obstacles before realizing the corresponding RT spintronics.[1] Therefore, two prerequisites should be fulfilled for realizing 100% spin polarized carriers at RT: (i) the electronic band structures should be nondegenerate with consequent large spin splitting; (ii) the Curie temperature (T_C) should be at least higher than RT.[1,19]

Although pristine halide perovskites (ABX_3, A = monovalent organic molecule or alkali metal, B = divalent carbon group cation and X = halogen anion) possess excellent optoelectronic properties, they usually exhibit no magnetism.[20–29] Náfrádi *et al.* reported Mn-doped $CH_3NH_3PbI_3$ with a weak magnetism, which suggests a promising route towards halide perovskite based spintronics.[30] However, the small spin splitting of less than 0.2 eV and low Curie temperature of lower than 15 K in their devices should be greatly improved before obtaining RT operated spintronics. Also, their adopted doping strategy could lead to aggregation and secondary phase separation of dilute magnetic materials. In contrast, intrinsic ferromagnetic semiconductors without any assistance of a doping strategy should

[a] *MIIT Key Laboratory of Advanced Display Materials and Devices, School of Materials Science and Engineering, Nanjing University of Science and Technology, Nanjing 210094, China. E-mail: zhangslvip@njust.edu.cn, zeng.haibo@njust.edu.cn*

[b] *Hefei National Laboratory for Physical Sciences at the Microscale, University of Science and Technology of China, Hefei, Anhui 230026, China*

† Electronic supplementary information (ESI) available. CCDC 1858498–1858518. For ESI and crystallographic data in CIF or other electronic format see DOI: 10.1039/c8mh00590g

be highly desirable in spintronic applications. Double perovskite oxides have been widely used for spintronic applications due to their simple crystal structures and consequent facile modelling, the large number of members of their elemental family as well as their tunable electronic and magnetic properties.[1] However, the magnetism of double perovskite halides (DPHs) has so far not been explored.

In this work, *via* first-principles calculations, we present a new class of Pb-free ferromagnetic (FM) DPHs with large spin splitting and ultrahigh T_C. Twenty-four types of Pb-free DPHs, namely Cs_2GeMX_6 (M = Ti, V, Cr, Mn, Fe, Co, Ni or Cu and X = Cl, Br, or I), have been investigated in detail, and ten of them exhibit good structure stability. Among the ten materials, based on the analysis of magnetic ground states and electronic properties, Cs_2GeMX_6 with M = V and Mn are FM semiconductors, and five of the FM DPHs have large spin splitting. Other DPHs, Cs_2GeMX_6 (M = Ti and Cr), are antiferromagnetic (AFM) materials. Moreover, all the FM compounds have Curie temperatures higher than 490 K, which is because DPHs possess a large number of nearest neighboring magnetic ions $z = 12$ and the strong exchange coupling between the M 3d and GeX_6 σ_{s-p}* orbitals. Furthermore, the T_C cannot be less than room temperature. Combining the good stability, nontoxic properties and large spin splitting together with ultrahigh T_C, Cs_2GeMnX_6 DPHs are promising candidates for spintronic applications.

Results and discussion

Crystallographic structures and magnetic ground states

Perovskites can usually exhibit four phases: cubic, tetragonal, orthorhombic and monoclinic. The cubic lattice is the most basic structure of perovskites, and the tetragonal lattice can be transferred to the cubic phase during the structure optimization. Moreover, the orthorhombic and monoclinic lattice can collapse in our simulation. Hence, we have mainly investigated the cubic lattice in this work. In cubic DPH $A_2B_IB_{II}X_6$ structures, each unit cell of DPH equals a 2 × 2 × 2 single perovskite supercell, which contains four B_IX_6 octahedrons and four $B_{II}X_6$ octahedrons. Two kinds of octahedrons alternately arrange along the three crystallographic axes, as shown in Fig. 1a. B_I and B_{II} atoms locate at the center of B_IX_6 and $B_{II}X_6$ octahedrons, respectively. B_I sites are occupied with the Ge element, because Ge-based perovskite halides have a similar formation energy to Pb-based perovskite halides, and both of them show better structure stability compared with Sn-based perovskite halides.[31] For B_{II} sites, transition metals are good candidates because of their unpaired d electrons, which usually lead to magnetism. The A sites locate at the octahedral interstice, which are filled with Cs ions. The reason for using Cs is that Cs can avoid the imposition of an arbitrary orientation for the organic group cation, and avoid the creation of a spontaneous polarization field in the organic group cations. The arbitrary orientation would increase the simulation difficulty, and the polarization field would affect the electronic properties. The optimized

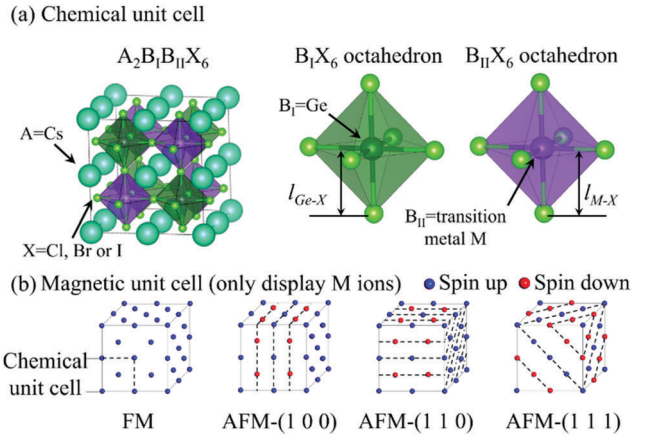

Fig. 1 (a) Crystalline structure of Cs_2GeMX_6. l_{Ge-X} and l_{M-X} are the Ge–X and M–X bond length, respectively. (b) Schematic illustration of the constructed FM coupling state and three AFM coupling states. The adopted magnetic unit cell is a 2 × 2 × 2 double perovskite supercell. Here, we only present magnetic M-site atoms. The blue and red colors denote the spin-up and spin-down M atoms, respectively.

lattice constants a, and bond lengths l_{Ge-X} and l_{M-X} are given in Table S1, ESI.†

To calculate the magnetic ground states of Cs_2GeMX_6, a magnetic unit cell was used to estimate the system energy, as shown in Fig. 1b. In these structures, the magnetic unit cell is defined as a 2 × 2 × 2 double perovskite supercell. We firstly construct one FM coupling state and three AFM coupling states. However, according to space and energy analysis, the AFM-(100) state is the same as AFM-(110). In terms of the total energy, Cs_2GeVX_6, Cs_2GeMnX_6, and Cs_2GeNiX_6 are FM states, while Cs_2GeTiX_6, Cs_2GeCrX_6, Cs_2GeFeX_6 and Cs_2GeCoX_6 are AFM, and Cs_2GeCuX_6 is nonmagnetic (NM), respectively. We further analyzed the electron configuration of M ions. The result could explain the difference between the magnetic ground state of DPHs. From Ti to Ni, the d orbitals are occupied by unpaired d electrons, which lead to a magnetic moment in M atoms, thereby giving rise to FM or AFM states. However, the 3d orbitals of Cu are occupied by five electron pairs. Thus, no spin magnetic moments can be found in Cs_2GeCuX_6, endowing the NM ground state in Cu-based DPHs.

Structure stability

Stability is a very important property of new materials. Here, we examine the different stabilities of DPHs through simulations. Firstly, effective tolerance factor t_{eff} and octahedral factor μ_{eff} were used to evaluate the crystallographic stability. Most of the DPHs locate in the area of $0.44 < \mu_{eff} < 0.90$ and $0.81 < t_{eff} < 1.11$, which indicates that they are crystallographically stable, as shown in Fig. 2a. The result also indicates that the cubic phase is the most suitable structure for our simulation, because perovskites tend to form the cubic phase when the tolerance factor t_{eff} is close to 1.[32,33] Secondly, we constructed different arrangement configurations of Cs_2GeMBr_6. The energy analysis indicates that the alternative arrangement of $GeBr_6$ and MBr_6 octahedrons is the most energetically

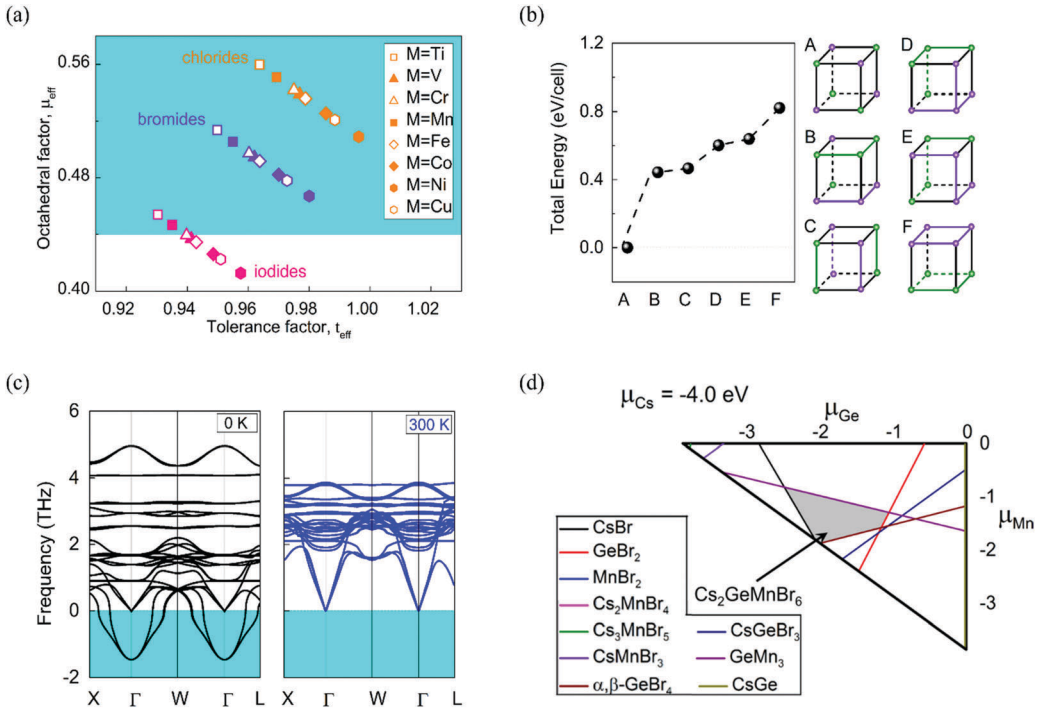

Fig. 2 (a) Distribution mapping of Cs_2GeMX_6 perovskites with different effective tolerance factors (t_{eff}) and octahedral factors (μ_{eff}). The stable region is highlighted by the cyan color. (b) Total energies of $Cs_2GeMnBr_6$ with different types of $GeBr_6$ (in gray) + $MnBr_6$ (in purple) motif arrangements. The lowest energy corresponding to configuration A was set to be zero. (c) Calculated phonon spectra at 0 K (left-hand side) and 300 K (right-hand side) of $Cs_2GeMnBr_6$. (d) Phase stability diagram analysis of double perovskite halides $Cs_2GeMnBr_6$. Only the slices at the chemical potential $\Delta\mu_{Cs}$ = −4.0 eV planes are shown here. The polygon region in gray represents thermodynamic stable conditions and each line corresponds to one competing phase.

favorable configuration, as shown in Fig. 2b. It is worth mentioning that other thermodynamic metastable phases may exist at finite temperatures since their energy differences are very small. Furthermore, the kinetic stabilities of DPHs are confirmed by phonon spectra, as shown in Fig. 2c. We can find soft modes, which indicate instability, in the 0 K phonon spectra. However, these soft modes disappear when the temperature rises up to 300 K. This result shows that DPHs exhibit the stable cubic phase at RT. Meanwhile, we find that the longitudinal optic–transverse optic (LO–TO) branch splitting feature at the gamma point is missing, which is caused by the high symmetry of cubic phase double perovskite halides. Herein, we do not discuss this point because LO–TO splitting is governed by different physics. Finally, we check the decomposition processes through phase diagram analysis. Fig. 2d shows slices of the polyhedron for stable $Cs_2GeMnBr_6$ in chemical potential μ_{Cs} = −4.0 eV. The complete data of phase diagram analysis are given in the ESI.† The gray regions in Fig. 2d can satisfy all chemical potential constraints, which means that high quality DPH samples without secondary competing phases can be realized in experiments. All results reveal that some DPHs are feasible in experiments.

Spin electronic properties

In order to understand the electronic and magnetic structures of all these systems, we analyzed the electronic configurations of AFM and FM DPHs, as shown in Fig. 3. Since the s electrons of the M atoms form bonds with the surrounding halogen atoms, only 3d electrons participate in orbital splitting in the octahedron crystal field and contribute to the magnetism. According to the crystal field theory, Hund's rule, the Pauli exclusion principle, and the Jahn–Teller (J–T) effect, the d orbitals could split into t_{2g} and e_g orbitals, and then further split into d_{xy}, d_{yz} and d_{zx} and $d_{x^2-y^2}$ and d_{z^2}. Only V with d^3 configuration, high spin Mn with d^5, and Ni with d^8 can avoid J–T distortions and have more effective coupling with surrounding atoms. As a result, V-based, Mn-based, and Ni-based DPHs display FM states.

The spin densities of Cs_2GeVBr_6, $Cs_2GeMnBr_6$ and $Cs_2GeNiBr_6$ are shown in Fig. 4. The result clearly indicates that the magnetism origin is M 3d orbitals (3 fold-degenerated t_{2g} for V, 3 fold-degenerated t_{2g} and 2-fold degenerated e_g for Mn and 2-fold degenerated e_g for Ni), which is in good agreement with the above discussions.

Because the main features of the GGA + U_{eff} electronic properties are the same as HSE06 (see ESI†), we discuss their electronic structures by using GGA + U_{eff} methods. Considering the toxic nature of V-based DPHs and the instability of Ni-based DPHs, we only displayed the spin-polarized band structure to study the bandgaps and spin splitting of FM ground state DPHs. The related information of the spin-polarized band structure of all FM ground state DPHs is shown in Table 1 and Fig. S3 in the ESI.† In terms of band structures, Cs_2GeMnX_6 DPHs are half semiconductors (HSCs, M = V, and Mn). HSCs refer to

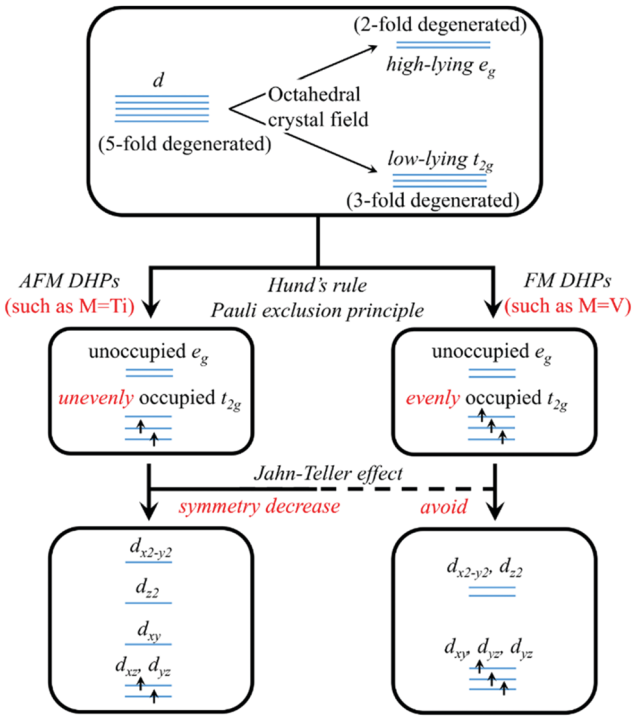

Fig. 3 (a) Diagram of the electronic configurations of transition metal M 3d orbitals. Unevenly occupied 3d orbitals would induce the Jahn–Teller effect, thereby giving rise to further splitting of t_{2g} and e_g orbitals. (b) Spin density of FM state Cs_2GeVBr_6, $Cs_2GeMnBr_6$ and $Cs_2GeNiBr_6$, respectively. The isovalue is 0.014 e Å^{-3}.

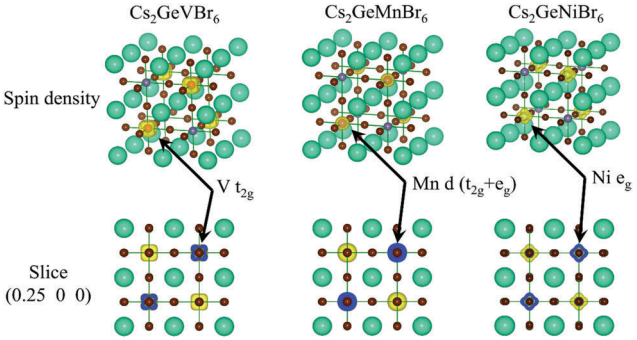

Fig. 4 Spin density of FM state Cs_2GeVBr_6, $Cs_2GeMnBr_6$ and $Cs_2GeNiBr_6$, respectively. The isovalue is 0.014 e Å^{-3}.

the semiconductors in one spin channel, whereas they are insulators in the other spin channels. Their valence band (VB) and conduction band (CB) are spin split with the valence band maximum (VBM) and conduction band minimum (CBM) possessing the same spin channel.

For Mn-based DPHs, the compounds are ferromagnetic semiconductors with the VBM and CBM occupied by the spin-up carriers, as shown in Fig. 5. The CBM is mainly dominated by the spin-up Ge p orbitals, and the VBM derives from the antibonding of the Mn e_g, Ge s, and X p orbitals. Cs_2GeMnX_6 (X = Cl, Br and I) has indirect bandgaps of 2.21 eV, 1.59 eV and 1.05 eV, respectively. As X changes from Cl, to Br, to I, the p orbital energy of X increases, leading to the lift of the VBM. The evolution of the VBM level accounts for the slightly decreasing profile of the band gap from 2.21 eV to 1.05 eV and ΔE_{VBM} from 0.86 eV to 0.20 eV. Moreover, the splitting can reach up to 0.86 eV, 0.78 eV and 0.43 eV for $Cs_2GeMnCl_6$, $Cs_2GeMnBr_6$ and Cs_2GeMnI_6, respectively. The half semiconductors are also ideal spintronic materials due to the presence of large spin splitting.

Table 1 The spin splitting (denoted by $\Delta E_{VBM} = E^{up}_{VBM} - E^{down}_{VBM}$ and $\Delta E_{CBM} = E^{up}_{CBM} - E^{down}_{CBM}$, in eV), nearest and next nearest exchange parameters J_1 and J_2 (in meV), energy band gaps (E_g, in eV), and magnetic moments per magnetic atom (M, in μ_B) for halide double perovskites by using the GGA + U_{eff} method

	ΔE_{CBM}	ΔE_{VBM}	E_g	J_1	J_2	M
Cs_2GeVCl_6	−0.40	1.00	2.26	−9.47	−1.37	3
Cs_2GeVBr_6	−0.30	0.71	2.04	−8.53	−1.24	3
Cs_2GeVI_6	−0.21	0.01	1.78	−7.40	−1.09	3
$Cs_2GeMnCl_6$	−0.35	0.86	2.21	−8.56	−3.75	5
$Cs_2GeMnBr_6$	−0.39	0.78	1.59	−7.76	−3.38	5
Cs_2GeMnI_6	−0.43	0.20	1.05	−6.82	−2.99	5
$Cs_2GeNiCl_6$	0.56	0.68	1.82	−6.15	−3.24	2
$Cs_2GeNiBr_6$	0.32	0.48	1.37	−5.50	−2.89	2
Cs_2GeNiI_6	0.09	0.06	0.97	−4.80	−2.52	2

Curie temperature

We now turn to study the magnetic properties of these compounds at finite temperatures. There are several mechanisms for the occurrence of long-range FM order at finite temperatures: barriers due to the nearest-neighboring number z of magnetic ions, the exchange integral J between two magnetic ions, and other factors in experiments. Here, the nearest-neighboring number z = 12 in DPHs is two times as much as that in double perovskite oxides (DPOs). This means that if the exchange integral J is equal in two systems, the spin flip needs to cross a higher barrier in DPHs. Thus, a long-range FM order can be stabilized at higher temperatures. Since z = 12 is a constant in these systems, we will not discuss more on this parameter. Large exchange integral J is critical to stabilize the long-range FM order. The nearest and the next nearest exchange parameter J_1 and J_2 can be extracted from the energy difference of the magnetic unit cell in Fig. 1b by using eqn (1)–(3). The data of J_1 and J_2 are listed in Table 1. The negative and positive J represent FM and AFM coupling, respectively.

$$E(\mathrm{FM}) = (192J_1 + 96J_2)|S|^2 \quad (1)$$

$$E(\mathrm{AFM1}) = (-64J_1 + 96J_2)|S|^2 \quad (2)$$

$$E(\mathrm{AFM2}) = -96J_2|S|^2 \quad (3)$$

$$H = -\sum_{\langle i,j\rangle} J_1 S_i \cdot S_j - \sum_{\langle k,l\rangle} J_2 S_k \cdot S_l \quad (4)$$

Then, we can extract T_C by performing the Ising model. In this model, the magnetic coupling Hamiltonian is expressed in eqn (4), in which the spin exchange parameter $J_{1,2}$ is the nearest and the next nearest exchange parameter, and $S_{i(,j,k,l)}$ is the total

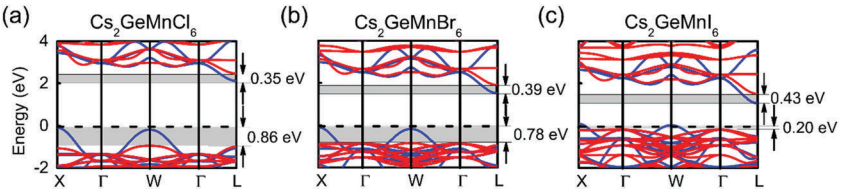

Fig. 5 Spin-polarized band structures of (a) $Cs_2GeMnCl_6$, (b) $Cs_2GeMnBr_6$ and (c) Cs_2GeMnI_6. Blue and red lines represent the spin-up and spin-down states, respectively. The width of the gray region represents the spin splitting value.

magnetic moment at site i (j, k, l). The Ising model is confirmed to provide good agreement with the experiments.[14] To estimate the T_C, we performed Monte Carlo (MC) simulation.[8,11,34] Our MC simulation is based on a 20 × 20 × 20 supercell, and the average magnetic moment per unit cell was extracted after the system reached equilibrium. Fig. 6 displays the magnetic moment of the systems as a function of temperature variation. It is clear to see that with an increase of the temperature, the magnetic moment of the system shows a sudden decrease at a certain temperature. This phenomenon indicates there is a magnetic phase transition and this temperature is the T_C. It can be seen that the T_C values of $Cs_2GeMnCl_6$, $Cs_2GeMnBr_6$, Cs_2GeMnI_6, Cs_2GeVCl_6, Cs_2GeVBr_6, Cs_2GeVI_6, $Cs_2GeNiCl_6$, $Cs_2GeNiBr_6$, and Cs_2GeNiI_6 are measured to be 800 K, 720 K, 640 K, 730 K, 660 K, 580 K, 640 K, 560 K, and 490 K, respectively.

From the above results, we know that DPHs can realize both semiconducting properties and high T_C. In general, the semiconductor characteristic is incompatible with high T_C. Why is the T_C of semiconductor DPHs much higher than RT?

Here, we take $Cs_2GeMnCl_6$ as an example to clarify the semiconductor characteristic. Previous study shows that the CBM and VBM of $CsM_{IVA}X_3$ (MIVA = Ge, Sn and Pb; X = Cl, Br and I) and $Cs_2M_{IVA}X_6$ are dominated by the M_{IVA} p orbitals and $M_{IVA}X_6$ σ_{s-p}* orbitals, respectively. The $M_{IVA}X_6^{4-}$ octahedron is the direct and main origin of semiconductor characteristics of $CsM_{IVA}X_3$ and $Cs_2M_{IVA}X_6$.[31] In these systems, semiconducting $GeCl_6$ groups were inserted into transition metal ions. This configuration can seriously limit carrier movements, thereby leading to semiconducting properties in the compounds. Since the bridging $GeCl_6^{4-}$ group in our work was different compared with the single-atom anion in the traditional superexchange, we identify it as the quasi superexchange coupling. The DHP crystal can remain semiconducting despite the interaction being strong between magnetic ions and nonmagnetic anions, because the octahedrons exhibit environment-independent semiconducting properties.

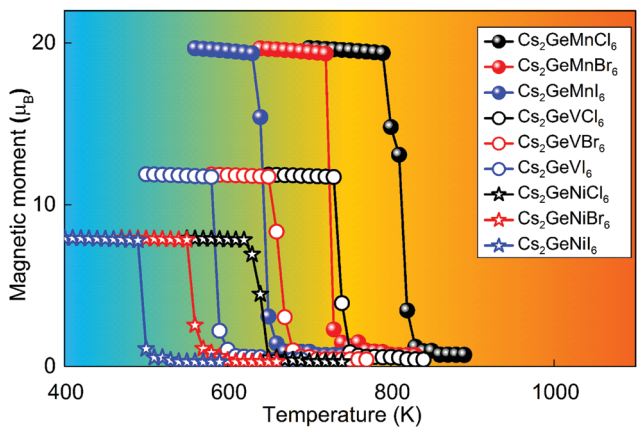

Fig. 6 Variation of the total magnetic moment per formula unit of Cs_2GeMX_6 (M = V, Mn, or Ni, X = Cl, Br, or I) as a function of temperature.

Then, we compared the difference between $Cs_2GeMnCl_6$ and Bi_2CrOsO_6 to study the origin of high T_C in DPHs. Exchange parameters are related by the coupling style. Since the distance between two nearest neighbor transition metal ions is larger than 7.0 Å, the direct coupling between them should be negligible. The indirect exchange coupling through the GeX_6 groups between two transition metal ions plays a majority role in ultrahigh T_C. From Fig. 7a, we can find a strong coupling between Mn 3d and Cl 4p orbitals. Hence, the indirect coupling can be described as a 90° quasi-superexchange model between the Mn 3d and $GeCl_6$ σ_{s-p}* orbitals, while the coupling model of DPOs is 180° superexchange of Cr(d)–O(p)–Os(d). The 90° superexchange interaction is more suitable for the ferromagnetic interaction compared to the 180° superexchange according to the Pauli exclusion principle. Exchange parameters are also determined by the overlap of charge distributions. Next, we calculated the electron location function (ELF) and deformation charge density (DCD) to analyse the indirect exchange coupling. The (110) plane was selected to analyse the ELF and DCD results because it contains four kinds of atoms in the quaternary compounds, as shown in Fig. 7b. Fig. 7c shows the ELF of two double perovskites, we observed that the maximum value locates at the Bi sites and the minimum value locates at the Cr/Os/O sites. In contrast, the maximum value and the minimum value are at the Ge/Cl and Cs/Mn sites in $Cs_2GeMnCl_6$. This evidence reveals that DPOs and DPHs have different bonding states. In other words, the iconicity of the M–GeX_6–M bond is stronger than the M–O–M bond with an increased electron density at the GeX_6 site than the O site. Fig. 7d shows the DCD of two kinds of double perovskites, we can see that there is charge depletion between the O and Os (Cr) atoms in Bi_2CrOsO_6. However, there is charge accumulation that can be found between Mn and the $GeCl_6$ groups in $Cs_2GeMnCl_6$. The charge depletion in Bi_2CrOsO_6 gives rise to the weaker overlap of charge distribution in DPOs than that in DPHs, resulting in a weaker exchange coupling in Os–O–Cr. Hence, the T_C of DPHs are much higher than Bi_2CrOsO_6 (201 K). Furthermore, the

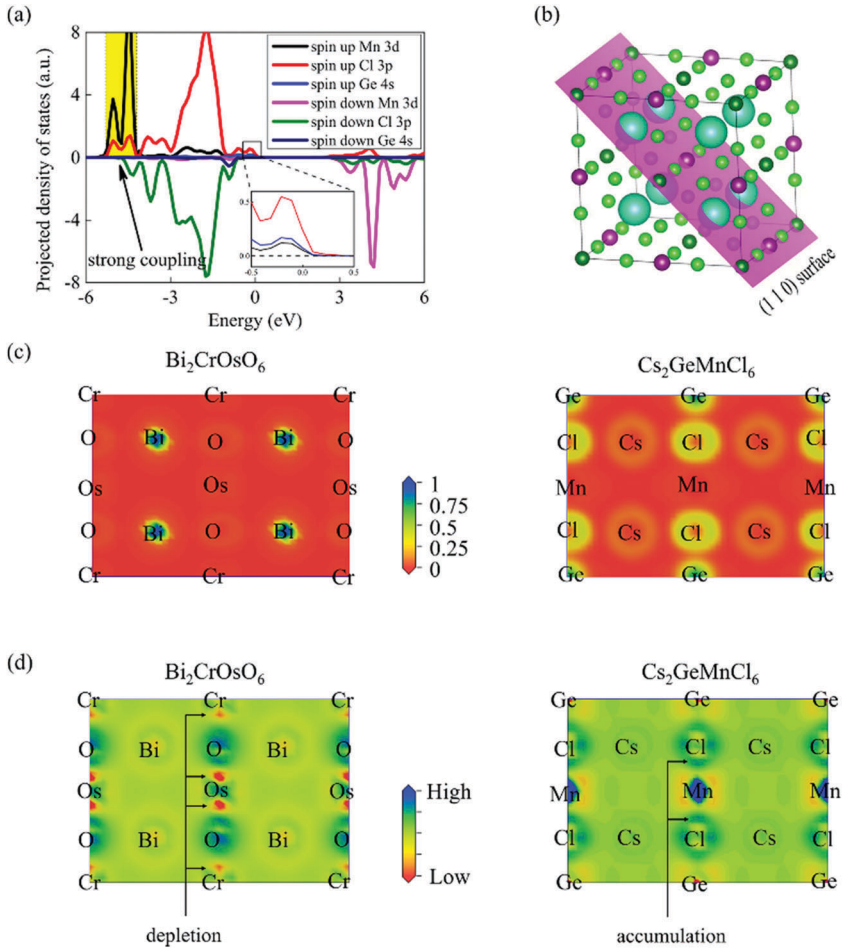

Fig. 7 (a) Orbital-projected density of states for $Cs_2GeMnCl_6$. All the Fermi levels are set to be zero. (b) The (110) plane (highlighted by purple) of the double perovskite structures, which contains all types of atoms. Maps of (c) the electron localization function (ELF) and (d) the deformation charge density for the DPO Bi_2CrOsO_6 and $Cs_2GeMnCl_6$ DPHs, respectively.

difference between the charge overlap cannot be used to clarify the bandgap. This is because the Bi atoms and Bi–O bonds affect significantly the Bi_2CrOsO_6 band structure, whereas the Cs atoms and Cs–Cl bonds do not have such effects.

We extracted the T_C by freezing the lattice constants in the above discussion. However, the lattice constant expansion (or contraction) is a common phenomenon, and a lot of factors can induce lattice constant change, such as interface lattice mismatch in devices and lattice thermal expansion. The lattice expansion could change the charge distribution, thereby affecting the exchange constant J. As a result, the result of T_C could change. Considering the toxic effect of the V element and the instability of Cs_2GeNiX_6, we do not supplement the calculation of Cs_2GeVX_6 and Cs_2GeNiX_6. Here, we only calculate the strain effect of Cs_2GeMnX_6 on T_C. In our calculation, the expansion ε is defined as

$$\varepsilon = \frac{a_0 - a}{a} \times 100\% \quad (5)$$

where a_0 is the expansion lattice constant and a is the equilibrium lattice constant. The negative value corresponds to the lattice contraction. The result is presented in Fig. 8. T_C shows a monotone decrease with increasing ε. With the lattice expansion, the overlap of charge distribution becomes weaker, which

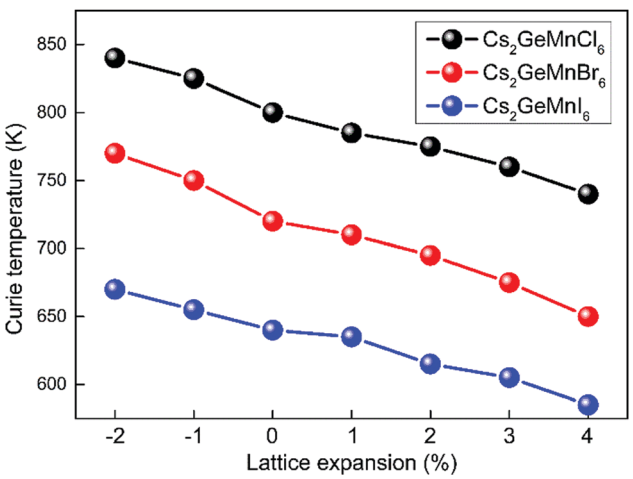

Fig. 8 Calculated lattice expansion effect on the T_C of Cs_2GeMnX_6.

would make the exchange coupling less effective. As a result, T_C can decrease with the lattice expansion and can remain higher than RT at a reasonable expansion effect.

Conclusions

In summary, *via* DFT calculations, we have presented a new class of semiconductor DPH Cs_2GeMX_6 with large spin splitting and high T_C. The DPH Cs_2GeMX_6 (M = Ti, V, Cr, Mn, Fe, Co, Ni, or Cu) exhibits a cubic lattice with GeX_6 and MX_6 alternating along the three crystallographic axes. Based on the calculation of the octahedral factor μ_{eff} and tolerance factor t_{eff}, along with the analysis of phonon spectra and the phase diagram, we found that ten of the twenty-four designed compounds possess good structural stability. Importantly, seven of the nine FM ground state DPHs have spin splitting larger than 0.4 eV and T_C in the range of 490–800 K. Moreover, the T_C can remain much higher than room temperature under the lattice expansion effect. Combining the excellent structural stability, nontoxic properties, large spin splitting and high T_C, Cs_2GeMnX_6 DPHs are the most ideal spintronic materials. Furthermore, we analyzed the origin of the semiconducting properties coupled with a high T_C. The semiconducting properties are caused by the alternating arrangement of magnetic transition metal ions and semiconducting groups. Moreover, the large number of nearest neighboring magnetic ions and the strong exchange coupling between the M 3d and GeX_6 σ_{s-p}* orbitals play a decisive role in the high T_C. Also, the mechanism analysis of the semiconductor characteristics coupled with high T_C could shed new light on the future design of advanced ferromagnetic semiconductors with tailored properties. In parallel with the current research into perovskite-based optoelectronics, our designed DPH semiconductors could open another intriguing route for the research of perovskite-based spintronics.

Conflicts of interest

There are no conflicts to declare.

Acknowledgements

This work was financially supported by the Fundamental Research Funds for the Central Universities (No. 30916015106), the National Basic Research Program of China (2014CB931702), the China Postdoctoral Science Foundation (AD41712) and the National Science Foundation for Distinguished Young Scholars of China (61725402). We thank Prof. Qiang Sun and Prof. Erjun Kan for fruitful discussions.

References

1 X. Li and J. Yang, *Natl. Sci. Rev.*, 2016, **3**, 365–381.
2 M.-R. Li, M. Retuerto, Z. Deng, P. W. Stephens, M. Croft, Q. Huang, H. Wu, X. Deng, G. Kotliar, J. Sánchez-Benítez, J. Hadermann, D. Walker and M. Greenblatt, *Angew. Chem., Int. Ed.*, 2015, **54**, 12069–12073.
3 T. S. Santos and J. S. Moodera, *Phys. Rev. B: Condens. Matter Mater. Phys.*, 2004, **69**, 241203.
4 J. Moodera, X. Hao, G. Gibson and R. Meservey, *Phys. Rev. Lett.*, 1988, **61**, 637.
5 X. Hao, J. Moodera and R. Meservey, *Phys. Rev. B: Condens. Matter Mater. Phys.*, 1990, **42**, 8235.
6 U. Lüders, A. Barthélémy, M. Bibes, K. Bouzehouane, S. Fusil, E. Jacquet, J. P. Contour, J. F. Bobo, J. Fontcuberta and A. Fert, *Adv. Mater.*, 2006, **18**, 1733–1736.
7 U. Lüders, M. Bibes, K. Bouzehouane, E. Jacquet, J.-P. Contour, S. Fusil, J.-F. Bobo, J. Fontcuberta, A. Barthélémy and A. Fert, *Appl. Phys. Lett.*, 2006, **88**, 082505.
8 S. Zhe-Wen and L. Bang-Gui, *Chin. Phys. B*, 2013, **22**, 047506.
9 X. Li, X. Wu, Z. Li and J. Yang, *Phys. Rev. B: Condens. Matter Mater. Phys.*, 2015, **92**, 125202.
10 P. Ravindran, R. Vidya, A. Kjekshus, H. Fjellvåg and O. Eriksson, *Phys. Rev. B: Condens. Matter Mater. Phys.*, 2006, **74**, 224412.
11 J. Wang, J. Meng and Z. Wu, *J. Comput. Chem.*, 2011, **32**, 3313–3318.
12 E. Solana-Madruga, Á. M. Arévalo-López, A. J. Dos Santos-García, E. Urones-Garrote, D. Ávila-Brande, R. Sáez-Puche and J. P. Attfield, *Angew. Chem., Int. Ed.*, 2016, **55**, 9340–9344.
13 A. M. Arévalo-López, G. M. McNally and J. P. Attfield, *Angew. Chem., Int. Ed.*, 2015, **54**, 12074–12077.
14 E. Şaşıoğlu, L. Sandratskii, P. Bruno and I. Galanakis, *Phys. Rev. B: Condens. Matter Mater. Phys.*, 2005, **72**, 184415.
15 C. Gong, L. Li, Z. Li, H. Ji, A. Stern, Y. Xia, T. Cao, W. Bao, C. Wang and Y. Wang, *Nature*, 2017, **546**, 265–269.
16 B. Huang, G. Clark, E. Navarro-Moratalla, D. R. Klein, R. Cheng, K. L. Seyler, D. Zhong, E. Schmidgall, M. A. McGuire, D. H. Cobden, W. Yao, D. Xiao, P. Jarillo-Herrero and X. Xu, *Nature*, 2017, **546**, 270–273.
17 X. Li and J. Yang, *J. Mater. Chem. C*, 2014, **2**, 7071–7076.
18 W.-B. Zhang, Q. Qu, P. Zhu and C.-H. Lam, *J. Mater. Chem. C*, 2015, **3**, 12457–12468.
19 K. Sato, L. Bergqvist, J. Kudrnovský, P. H. Dederichs, O. Eriksson, I. Turek, B. Sanyal, G. Bouzerar, H. Katayama-Yoshida and V. Dinh, *Rev. Mod. Phys.*, 2010, **82**, 1633.
20 W.-J. Yin, J.-H. Yang, J. Kang, Y. Yan and S.-H. Wei, *J. Mater. Chem. A*, 2015, **3**, 8926–8942.
21 G. Giorgi and K. Yamashita, *Chem. Lett.*, 2015, **44**, 826–828.
22 H.-J. Feng, T. R. Paudel, E. Y. Tsymbal and X. C. Zeng, *J. Am. Chem. Soc.*, 2015, **137**, 8227–8236.
23 R. Dong, Y. Fang, J. Chae, J. Dai, Z. Xiao, Q. Dong, Y. Yuan, A. Centrone, X. C. Zeng and J. Huang, *Adv. Mater.*, 2015, **27**, 1912–1918.
24 C. Huo, B. Cai, Z. Yuan, B. Ma and H. Zeng, *Small Methods*, 2017, **1**, 1600018.
25 X.-G. Zhao, J.-H. Yang, Y. Fu, D. Yang, Q. Xu, L. Yu, S.-H. Wei and L. Zhang, *J. Am. Chem. Soc.*, 2017, **139**, 2630–2638.
26 X.-G. Zhao, D. Yang, Y. Sun, T. Li, L. Zhang, L. Yu and A. Zunger, *J. Am. Chem. Soc.*, 2017, **139**, 6718–6725.
27 X. Liu, D. Yu, F. Cao, X. Li, J. Ji, J. Chen, X. Song and H. Zeng, *Small*, 2017, **13**, 1700364.
28 Z. Xiao, W. Meng, J. Wang, D. B. Mitzi and Y. Yan, *Mater. Horiz.*, 2017, **4**, 206–216.

29 T. T. Tran, J. R. Panella, J. R. Chamorro, J. R. Morey and T. M. McQueen, *Mater. Horiz.*, 2017, **4**, 688–693.
30 B. Náfrádi, P. Szirmai, M. Spina, H. Lee, O. Yazyev, A. Arakcheeva, D. Chernyshov, M. Gibert, L. Forró and E. Horváth, *Nat. Commun.*, 2016, **7**, 13406.
31 P. P. Sun, Q. S. Li, L. N. Yang and Z. S. Li, *Nanoscale*, 2016, **8**, 1503.
32 Z. Li, M. Yang, J.-S. Park, S.-H. Wei, J. J. Berry and K. Zhu, *Chem. Mater.*, 2016, **28**, 284–292.
33 M. R. Filip, G. E. Eperon, H. J. Snaith and F. Giustino, *Nat. Commun.*, 2014, **5**, 5757.
34 F. Wu, C. Huang, H. Wu, C. Lee, K. Deng, E. Kan and P. Jena, *Nano Lett.*, 2015, **15**, 8277–8281.